Supporting Information for:

Aqueous Chemistry of MoS_2 Nanopores: How Functional Groups Influence Water Permeability and Ion/Boron Rejection

Pradeep Dhondi and Ananth Govind Rajan*

Department of Chemical Engineering, Indian Institute of Science, Bengaluru, Karnataka 560012, India

*Corresponding Author (Email: ananthgr@iisc.ac.in)

Table of Contents

S1. Details of the density functional theory simulations

We started by optimizing the plane wave cutoff (E_CUT) and relative cutoff (REL_CUT) using a 1 meV/atom energy convergence criterion, utilizing the cp2k package for DFT calculations. A 6×6×3 k-point mesh was used during optimization. The effect of nuclei and core electrons in the system was modeled using Goedecker-Teter-Hutter pseudopotentials[1] and double-zeta (short-range) MOLOPT basis sets were used to represent the valence electron wavefunction and density. The Perdew-Burke-Ernzerhof (PBE) exchange-correlation functional[2] was employed in the simulations. Following that, the unit cell of 2H-MoS_2 with AB stacking was optimized (i.e., the *a*, *b*, and *c* lattice parameters were obtained) by setting the maximum force criteria on all atoms as $0.0003\,\frac{\text{hartree}}{\text{bohr}}$ with E_CUT= 400 Ry, REL_CUT = 40 Ry (obtained from energy convergence). The equilibrium lattice parameters in our study, obtained from cell optimization, are $a = b = 3.16382$ Å and $c = 12.200425$ Å, in good agreement with the experimental values[3] of $a = b = 3.16$ Å and $c = 12.294$ Å. After cell optimization was carried out, we used the optimized *a*, *b*, and *c* values to make a supercell consisting of 90 atoms with Mo and S atoms for force-field fitting. While a typical supercell exposes both zigzag and armchair edges with Mo and S terminations (Figure S1), in our study, we considered zigzag edges, as these are commonly observed in MoS_2 sheets and are energetically stable edge orientations.[4,5] As shown in Figure S1, the zigzag edges of the MoS_2 sheet, including the S edge (with S atoms on the edges) and the Mo edge (with Mo atoms on the edges), were then functionalized with H and O/OH groups, respectively. After functionalization, we carried out geometry optimization for the functionalized MoS_2 sheet using the Broyden-Fletcher-Goldfarb-Shanno algorithm by setting the maximum force criterion on any atom to be $0.0003\,\frac{\text{hartree}}{\text{bohr}}$.

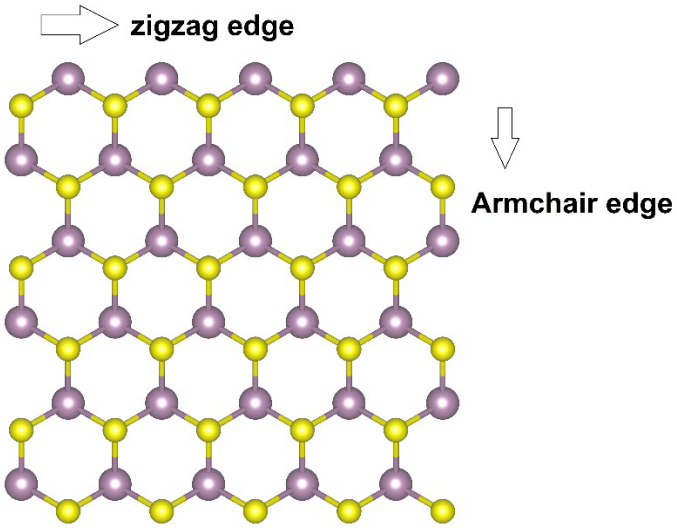

Figure S1. 2H MoS_2 sheet consisting of 90 atoms with zigzag and armchair edges labeled. Color code: Mo: purple, S: yellow.

Following geometry optimization, the resulting structures were used to calculate partial atomic charges. These charges were derived using the DFT-based density-derived atomic point (DDAP) charge fitting method, as implemented in cp2k and originally developed by Blöchl[6]. The DDAP approach relies on several key parameters specified in the DENSITY_FITTING section of cp2k, including GCUT (cutoff for charge fitting in G-space), NUM_GAUSS (number of Gaussian functions used to fit the quantum-mechanical charge density at each atomic site), PFACTOR (progression factor for the Gaussian exponents), and MIN_RADIUS (minimum radius of the Gaussians). These parameters were carefully selected to obtain accurate partial charges for all relevant atoms (Mo, S, O, and H; shown in Table S1). To evaluate the electrostatic potential generated by these charges, the total electrostatic potential was computed on a real-space grid using the V_HARTREE_CUBE option in cp2k, which outputs the potential as a cube file. To validate the DDAP-derived partial charges, we performed single-point energy calculations in LAMMPS by moving a unit test charge along the direction normal to the MoS_2 surface. In these calculations, the relaxed MoS_2 structure from DFT and the corresponding DDAP charges were used to compute the electrostatic interaction energy between the test charge and the MoS_2 layer. The electrostatic potential obtained from these LAMMPS simulations via the group/group command was then compared with the DFT-derived potential profile. Although the two profiles exhibit similar shapes and trends, a mismatch in magnitude is observed. This arises because the DDAP model density is constructed from atom-centered spherically symmetric Gaussian basis functions and is fitted

only to the low-G components of the electron density, which determine the long-range electrostatics. Since higher-G features are responsible for the short-range anisotropy and higher-order multipole characteristics of the density are not captured within this representation, the electrostatic potential reconstructed from the DDAP-derived charges deviates in magnitude from the full DFT potential, even though the overall profile remains qualitatively similar. This incomplete representation can lead to systematic deviations in the electrostatic potential reconstructed from the assigned charges, especially in chemically anisotropic environments. To reconcile this difference, a uniform scaling factor was applied to the DDAP charges, enabling better agreement between the MD-derived and DFT-calculated electrostatic potentials. The scaling factor for different pore geometries is detailed in the following section (Table S2). These rescaled charges were subsequently used in MD simulations to investigate water permeation and ion rejection across various MoS_2 nanopore models.

Table S1. DDAP parameters used in the current study for various configurations.

Case	GCUT	NUM_GAUSS	PFACTOR	MIN_RADIUS
OH-, O-, and H-functionalized Mo and S zigzag edges for force-field fitting	2.449	4	1.31	0.264589
S (Triangular pore)	2.499	5	1.5	0.264589
Mo (Triangular pore)	2.449	3	1.31	0.529177
Mo-OH (Triangular pore)	2.449	5	1.31	0.264589
S and Mo (Hexagonal pore)	2.499	3	1.5	0.529177
S-H and Mo-O (Hexagonal pore)	2.499	5	1.31	0.264589

To achieve quantitative agreement between the electrostatic potential derived from DFT and that obtained using DDAP-based partial charges, we applied a uniform rescaling to the DFT-predicted atomic charges for various nanopores. No rescaling was used during force-field fitting. Before rescaling, both the DFT and partial-charge-based electrostatic potential profiles were aligned by shifting them such that the potential at the boundary of the simulation box along the axis normal to the MoS_2 surface was zero. This shifting ensured a consistent baseline for comparison. The scaling factor, denoted as α, was determined as the ratio between the maximum value of the DFT electrostatic potential and the

maximum value of the partial charges-based potential obtained using the unscaled DDAP charges (q_{DDAP}):

$$\alpha = \frac{|(\text{max potential})_{\mathrm{DFT}}|}{|(\text{max potential})_{\text{partial charges}}|}$$

This method was only implemented when the DFT and partial-charge-based potential profiles exhibited similar spatial distributions, differing primarily in magnitude. The rescaled charges (q_{scaled}) used in the MD simulations were then computed as:

$$q_{\mathrm{scaled}} = \alpha q_{\mathrm{DDAP}}$$

These adjusted charges were subsequently used to model electrostatic interactions in classical MD simulations, ensuring a closer match to the DFT-derived potential landscape and thereby improving the accuracy of water transport and ion rejection predictions across the MoS_2 nanopores. More detailed information regarding the DDAP rescaling procedure can be found in our previous publication.[7]

Table S2. Charge rescaling factors for various pore types.

Pores	Rescaling factor α
S (Triangular pore)	1.4781
Mo (Triangular pore)	0.666
Mo-OH (Triangular pore)	1.102
S and Mo (Hexagonal pore)	0.3339
S-H and Mo-O (Hexagonal pore)	1.1667

S2. Partial charges employed for various nanopores, effect of partial charge calculation scheme, and tabulated sizes of various nanopores considered

The partial charges employed in the MD simulations for all the nanopores considered in this work are shown in Figure S2. Regarding the partial charge scheme employed, we observed that density-derived electrostatic and chemical (DDEC)[8,9] charges do not accurately reproduce the electrostatic potential across the nanopore when compared to DDAP charges. For instance, in the case of an unfunctionalized triangular S pore, the potential profiles obtained from DFT and point charges are reversed when using DDEC charges, an inconsistency that is not present when using DDAP charges, as shown in Figure S3.

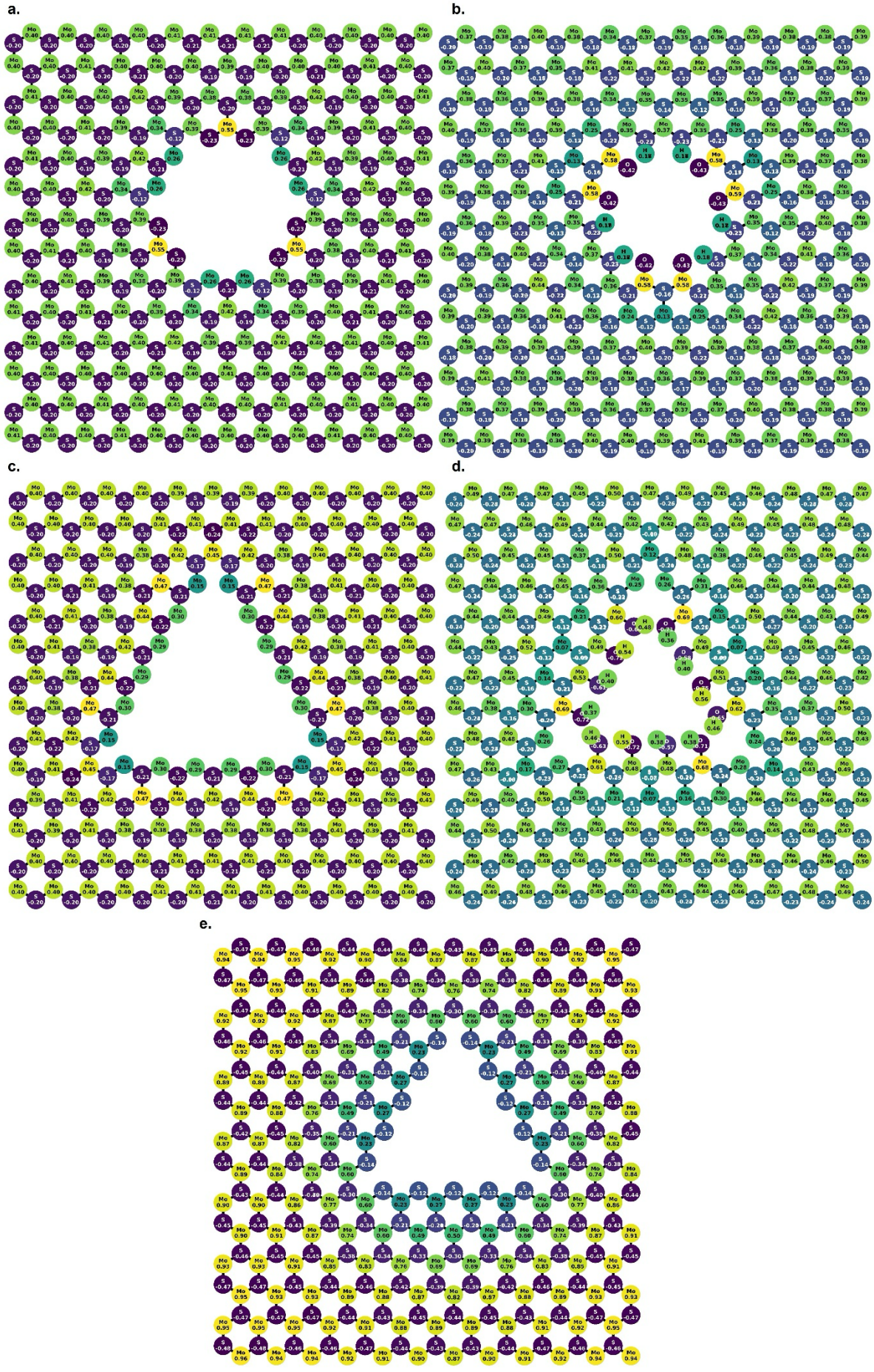
a.
b.
c.
d.
e.

Figure S2. Rescaled partial charge distribution (in elementary charge units, e) computed using the DDAP scheme for (a) unfunctionalized hexagonal pore, (b) functionalized hexagonal pore, (c) unfunctionalized triangular Mo-terminated pore, (d) functionalized triangular Mo-terminated pore, and (e) unfunctionalized triangular S edge pore.

Therefore, in this study, we primarily focus on and discuss the results obtained with DDAP charges. Nevertheless, the results obtained using DDEC charges are illustrated in Figure S4. Although MD simulations with DDEC charges were stable, they showed similar outcomes to the results based on DDAP charges, that unfunctionalized S-terminated triangular pores provide high water permeance with excellent salt rejection, while functionalized hexagonal pores and Mo-terminated triangular pores also achieve high water permeance while maintaining salt rejection.

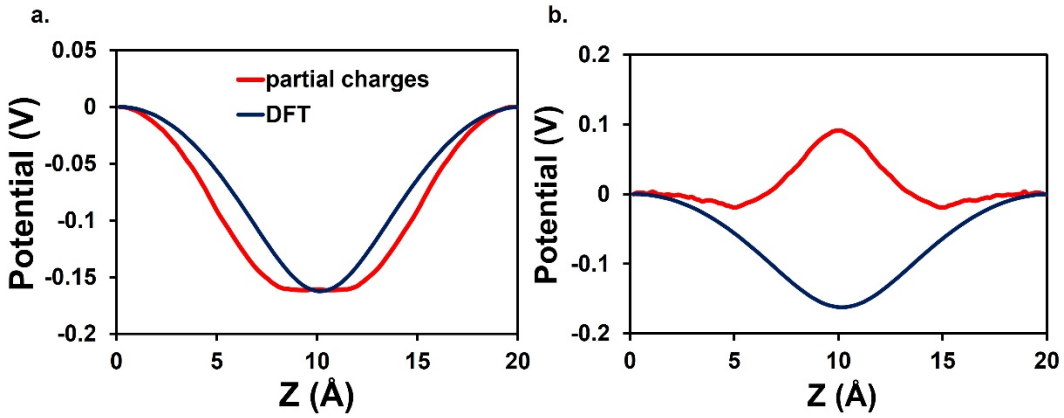

Figure S3. Partial-charge-based potential (labeled MD) and DFT potential for unfunctionalized S edge nanopore with two different charge schemes: (a) DDAP and (b) DDEC.

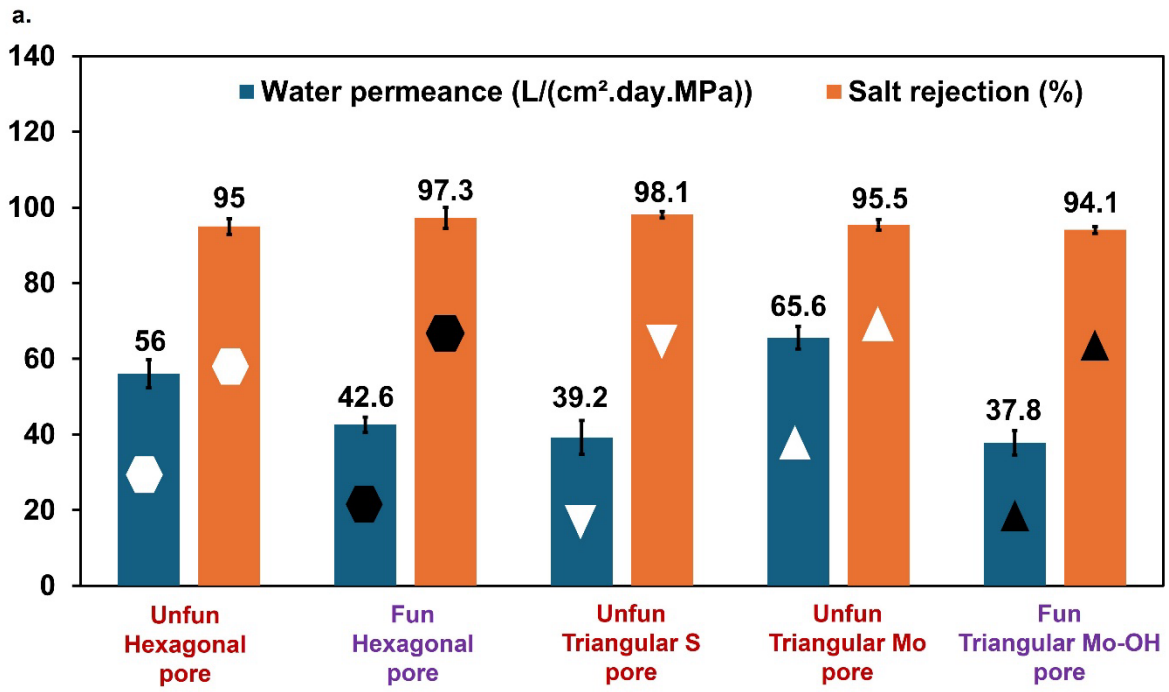

Figure S4. MD simulation results for NaCl aqueous salt solution separation for different pore geometries used in MoS_2 membranes with DDEC charges. (a) Water permeance ($L.cm^{-2}.day^{-1}.MPa^{-1}$) rates and overall salt rejection from the feed side to permeate side for nanopores with functionalized ("Func.") and unfunctionalized ("Unfunc.") Mo and S-terminated hexagonal. Note that the symbols inside the bars indicate pore geometry and chemistry: hexagonal and triangular markers represent hexagonal and triangular pores, respectively. Filled (solid black) markers denote functionalized nanopores, whereas unfilled (white) markers denote unfunctionalized nanopores. Upward (▲) and downward (▼) triangles correspond to Mo-terminated and S-terminated triangular pores, respectively.

The procedure employed for fitting the force-field parameters is provided in Figure S5.

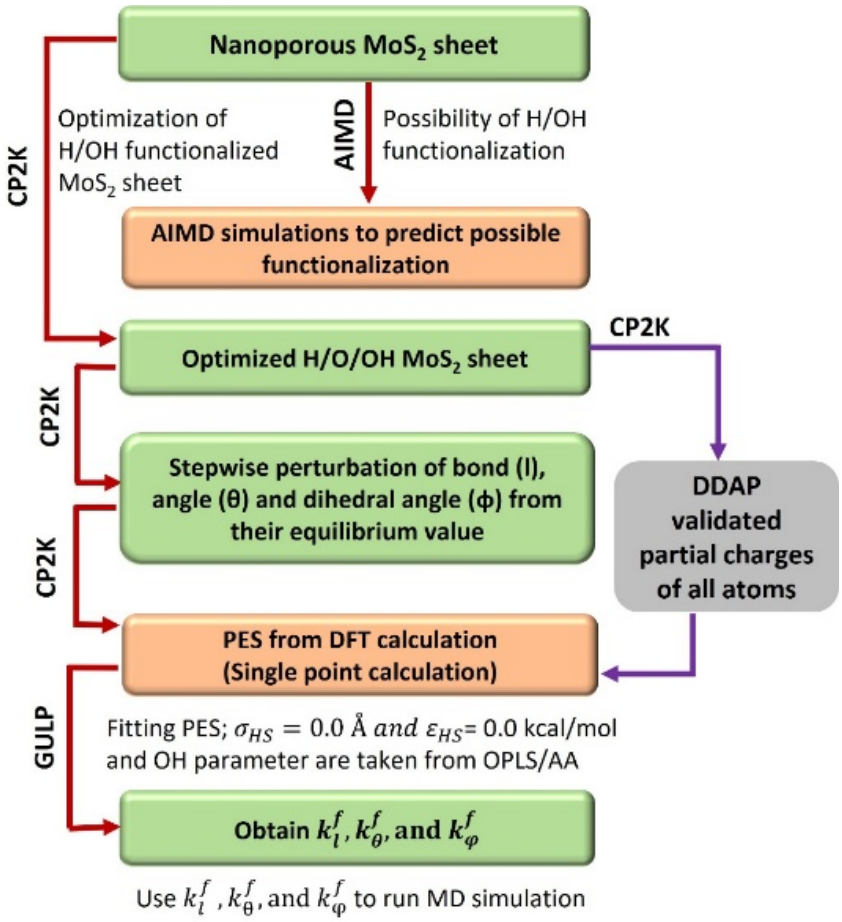

Figure S5. The step-by-step process for force field (FF) development, along with the codes used at each step.

S2. Details of the force-field parameters adapted from previous work

The Lennard-Jones parameters and partial charges adapted from previous work into this study are provided in Table S3. The partial charges for Mo, S, hydrogen bonded to sulfur (HS), oxygen bonded to Mo (OMo), and hydrogen in hydroxyl (HO) are calculated using DFT with the density-derived atomic point (DDAP) method implemented in cp2k.

Table S3. Force-field parameters of various atoms adapted from previous work.

Atoms	σ (Å)	$\epsilon \left(\frac{\text{kJ}}{\text{mol}}\right)$	*q (e)*	*Reference*
Na^+ (Salt)	2.21737	1.472356	0.85	Zeron et al.[10]
Cl^- (Salt)	4.69906	0.076923	-0.85	Zeron et al.[10]
C (Piston)	3.4	0.2331456	0.0	Cheng and Steele[11]
Mo (Membrane)	4.34	0.485	Obtained from DDAP	Govind Rajan et al.[12]
S (Membrane)	3.34	2.085	Obtained from DDAP	Govind Rajan et al.[12]
H (Water)	0.0	0.0	0.5564	Abascal et al.[13]
O (Water)	3.1589	0.7748768	-1.1128	Abascal et al.[13]

S4. Effect of ensemble choice: NVT compared with $NP_{xy}T$

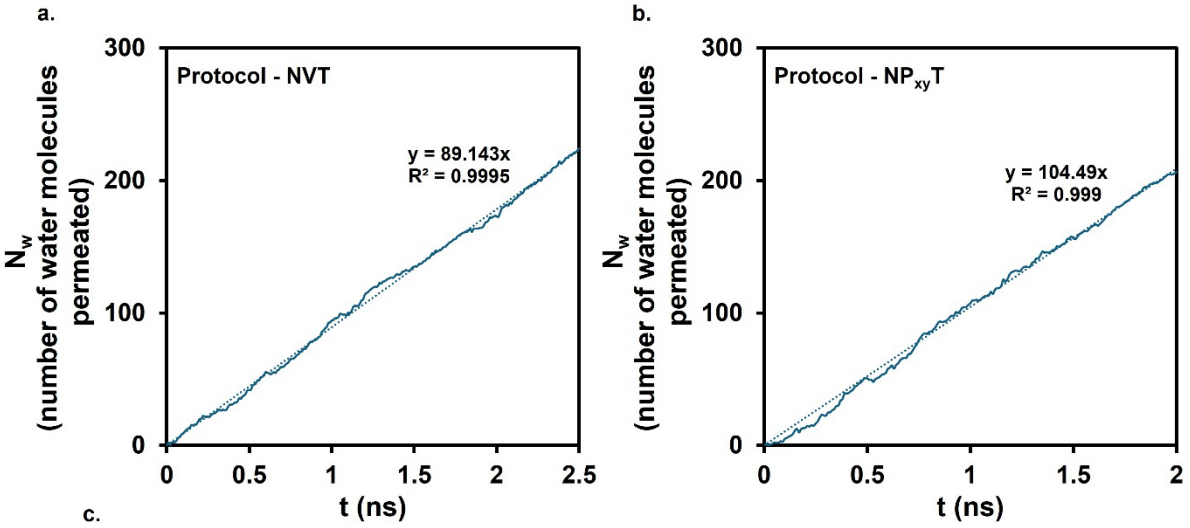

c.

Triangular S terminated pore	Protocol - NPxyT	Protocol - NVT
Water permeance ($L.cm^{-2}.day^{-1}.MPa^{-1}$)	43.4 ± 3.3	35.6 ± 2.0
Salt rejection (%)	99.2 ± 0.5	99.3 ± 0.4

Figure S6. Influence of ensemble selection on desalination performance. (a) The number of water molecules permeated with simulation time using the *NVT* ensemble protocol. (b) The number of water molecules permeated with simulation time using the $NP_{xy}T$ ensemble protocol. (c) Water permeance and salt rejection for both *NVT* and $NP_{xy}T$ protocols.

S5. Discussion of the AIMD simulation results

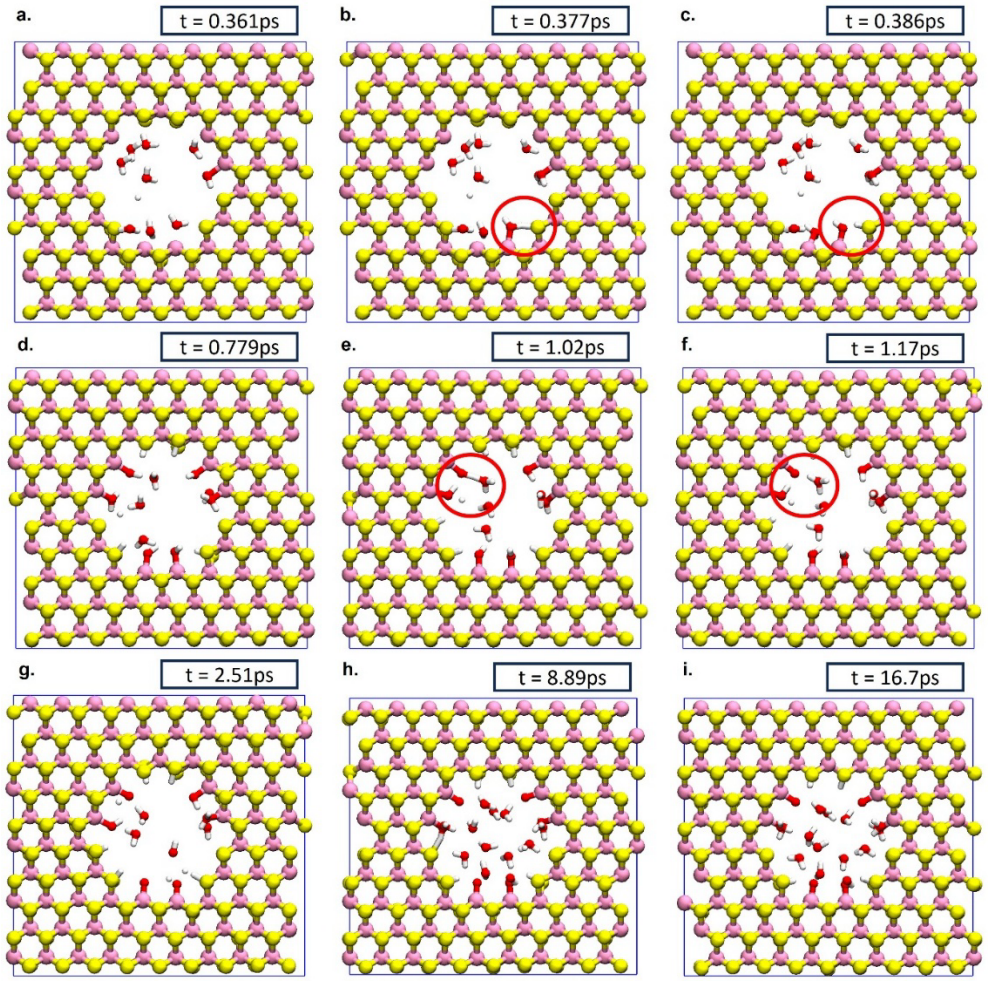

Figure S7. Non-spin polarized AIMD simulation snapshots of the functionalization of a hexagonal pore configuration, where both Mo and S atoms are exposed to the water medium. The simulation time corresponding to each snapshot is indicated in the top right corner. Only showing Mo, S, O, and H atoms within 14 Å < z < 18.5 Å to highlight the edge functional groups, with the 2D MoS_2 membrane located in the region 14.6 Å < z < 17.6 Å. Important transitions are marked with red circles in the respective snapshots. Color code: Mo: purple, S: yellow, H: white, O: red.

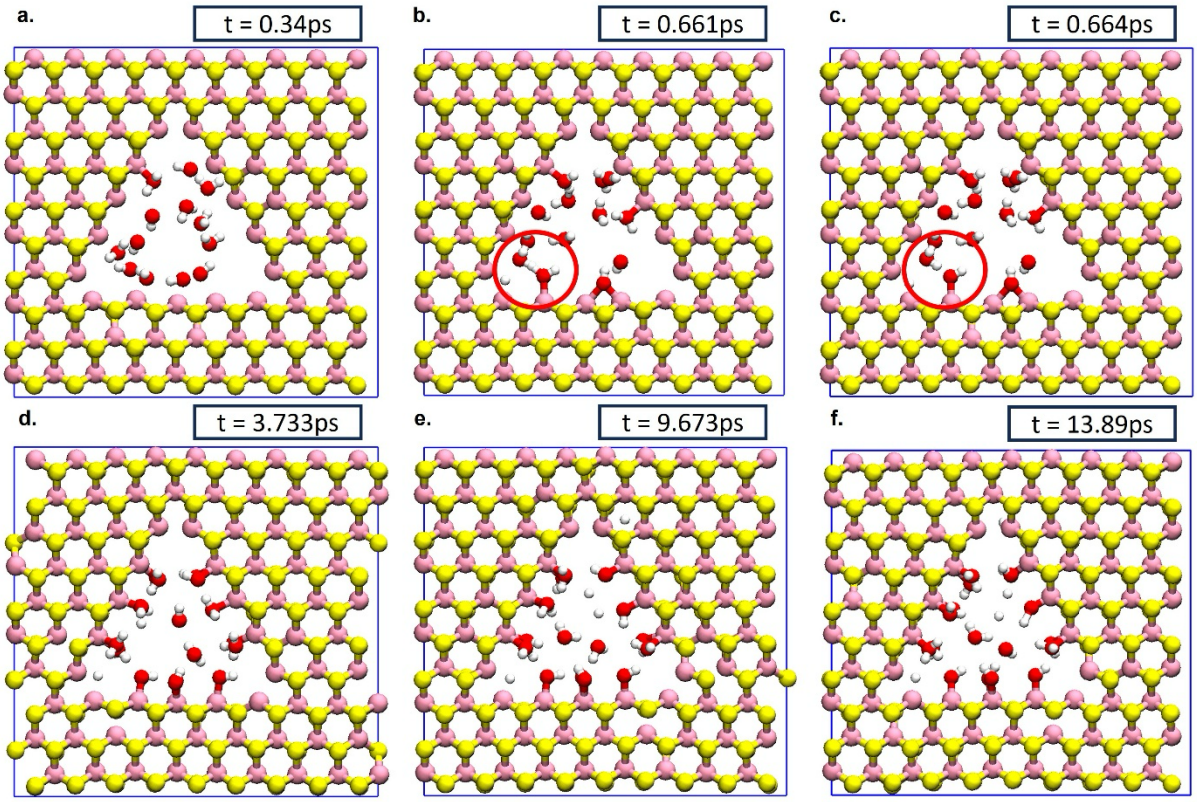

Figure S8. Non-spin polarized AIMD simulation snapshots of functionalization of a triangular pore configuration, where only Mo atoms are exposed to the water medium. The simulation time corresponding to each snapshot is indicated in the top right corner. Only showing Mo, S, O, and H atoms within 14 Å < z < 18.5 Å to highlight the edge functional groups, with the 2D MoS_2 membrane located in the region 14.6 Å < z < 17.6 Å. Important transitions are marked with red circles in the respective snapshots. Color code: Mo: purple, S: yellow, H: white, O: red.

Our AIMD simulation of the triangular pore shows that at around 0.34 ps, a water molecule from the bulk adsorbs onto a Mo atom without dissociating (Figure S8a). Later, at approximately 0.661 ps, a nearby water molecule pulls a proton from one of the adsorbed water molecules, triggering its dissociation into H^+ and OH^-. The released proton transfers to the nearby water molecule, forming H_3O^+, while the remaining OH. binds to the Mo atom (Figure S8b,c). Snapshots at 3.733 ps and 9.673 ps show four Mo atoms each bonded to OH groups. This process of proton transfer and bond formation continues over the next 41 ps, eventually leading to six Mo-OH bonds and the non-dissociative adsorption of three additional water molecules on Mo atoms (Figure 2).

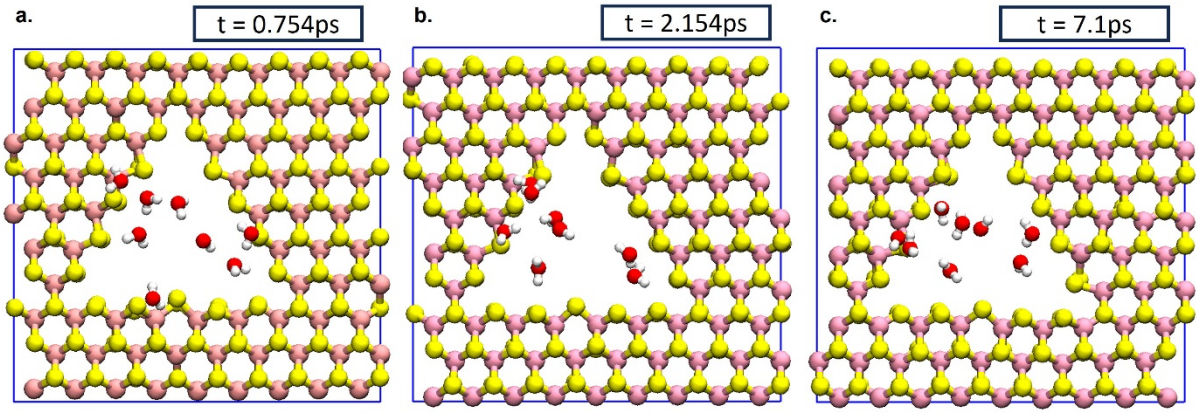

Figure S9. Non-spin polarized AIMD simulation snapshots of functionalization of a triangular pore configuration, where only S atoms are exposed to the water medium. The simulation time corresponding to each snapshot is indicated in the top right corner. Only showing Mo, S, O, and H atoms within 14 Å $< z <$ 18.5 Å to highlight the edge functional groups, with the 2D MoS_2 membrane located in the region 14.6 Å $< z <$ 17.6 Å. Color code: Mo: purple, S: yellow, H: white, O: red.

AIMD simulations of a triangular S-terminated pore show that, in contrast to the Mo-exposed triangular pore, when only S edge atoms were exposed, no bond formation or functionalization occurred throughout the simulation, suggesting that sulfur alone does not readily react with water under these conditions. Snapshots taken at 0.75 ps, 2.154 ps, and 7.1 ps (Figure S9a-c) consistently show that water molecules approach the pore edge and form hydrogen-bonded networks with water on the opposite side, enabling them to pass through the pore without interacting chemically with the sulfur sites or undergoing dissociation. This lack of reactivity can be attributed to the absence of nearby Mo atoms, which appear to play a critical role in attracting water molecules to the pore edge, facilitating water dissociation, and enabling subsequent proton transfer to sulfur. By the end of the 14 ps simulation, no S-edge functionalization or bond formation was observed. The AIMD results for different nanopores are in line with the results of Ghuman et al., who used DFT and AIMD[14] and showed that when Mo-terminated edges (0% sulfur) are exposed, water readily dissociates because undercoordinated Mo atoms strongly attract and polarize H_2O molecules, leading to the formation of OH and Mo-O bonds. In contrast, when sulfur-terminated edges are exposed, water neither adsorbs nor dissociates readily, making them largely inert toward water splitting. However, they reported that S-H bond formation is thermodynamically feasible if hydrogen is already available, rather than produced in situ from water.

Comparison with spin-polarized AIMD simulations

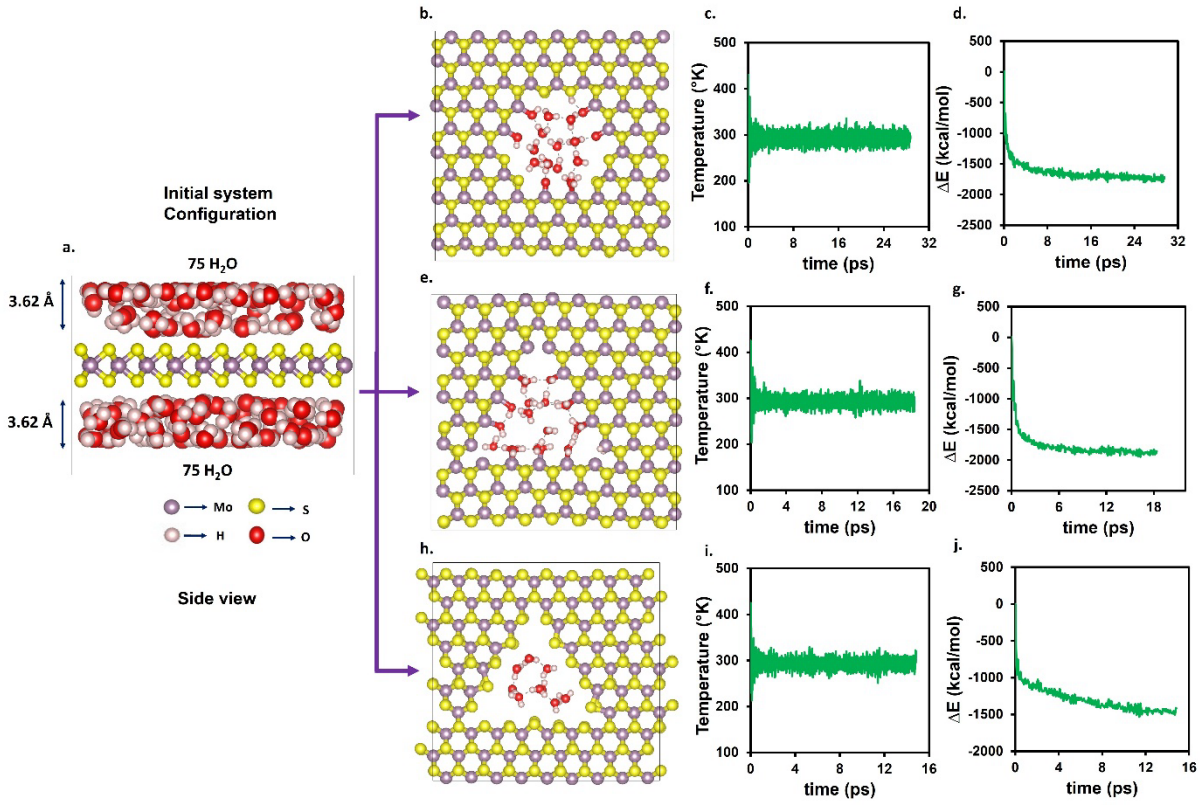

Figure S10. Spin-polarized AIMD simulation setup used to probe MoS_2 functionalization and the ensuing results. (a) Side view of the initial setup showing a nanoporous MoS_2 sheet positioned between two water slabs. (b) Snapshot after 28 ps of AIMD simulation for a hexagonal pore with Mo- and S-terminated edges. (c) Temperature fluctuations over simulation time for the hexagonal pore. (d) DFT relative energy for different configurations with respect to the initial frame over simulation time for the hexagonal nanopore. (e) Snapshot after 18 ps of AIMD simulation for a triangular pore with Mo-terminated edges. (f) Temperature fluctuations over the simulation time for the Mo-terminated triangular pore. (g) DFT relative energy for different configurations with the initial frame over simulation time for the Mo-terminated triangular nanopore. (h) Snapshot after 15 ps of AIMD simulation for a S-terminated triangular pore. (i) Temperature fluctuations over the simulation time for the S-terminated triangular pore. (j) DFT relative energy for different configurations with the initial frame over simulation time for the S-terminated triangular nanopore. Color code: Mo: purple, S: yellow, H: white, O: red. In each case, we show Mo, S, O, and H atoms within 14 Å < z < 18.5 Å to highlight the edge functional groups, with the 2D MoS_2 membrane located in the region 14.6 Å < z < 17.6 Å

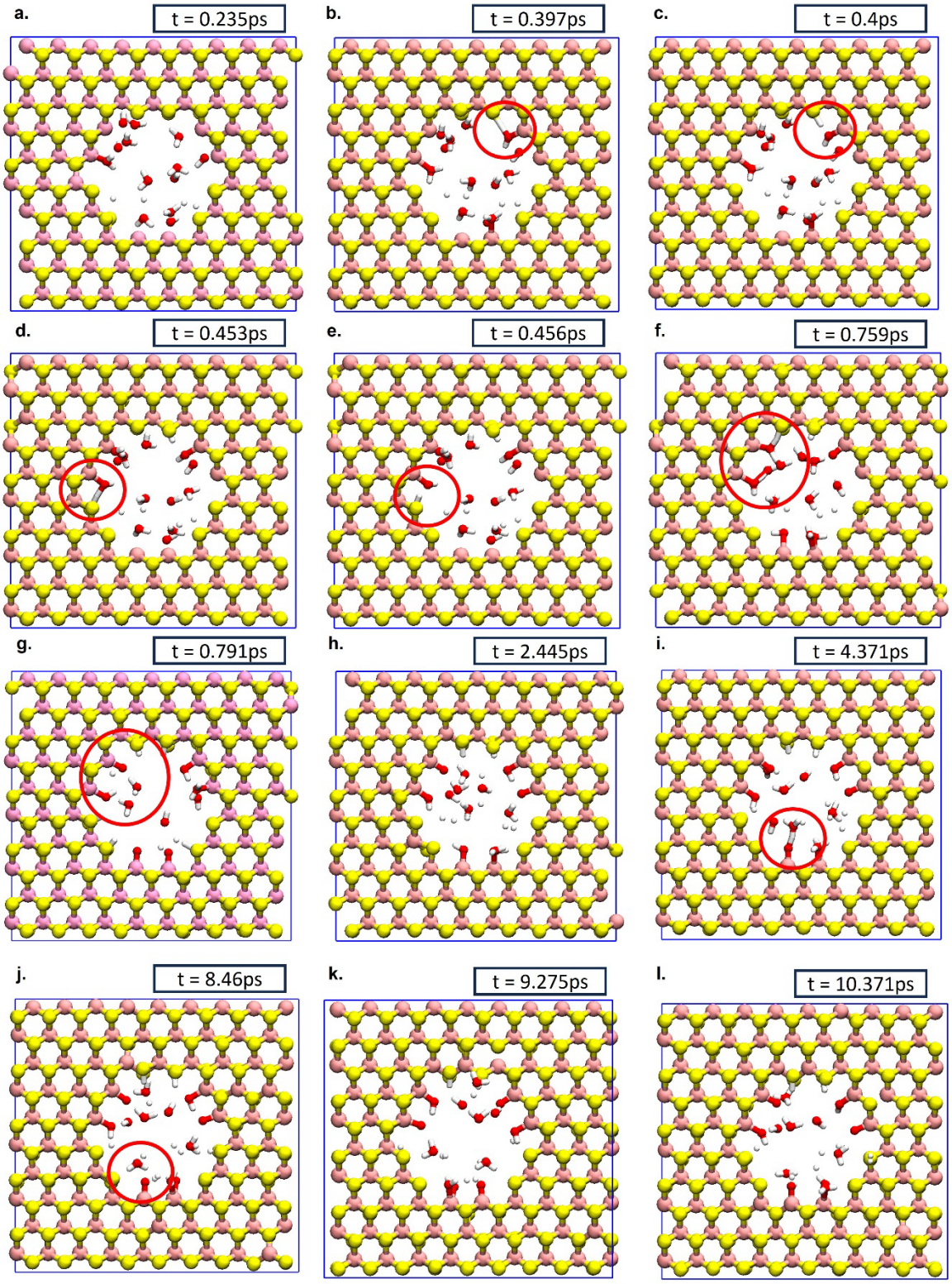

Figure S11. Spin-polarized AIMD simulation snapshots of the functionalization of a hexagonal pore configuration, where both Mo and S atoms are exposed to the water medium. The simulation time corresponding to each snapshot is indicated in the top right corner. We only show the Mo, S, O, and H atoms within 14 Å < z < 18.5 Å to highlight the edge functional groups, with the 2D MoS_2 membrane located in the region 14.6 Å < z < 17.6 Å. Important transitions are marked with red circles in the respective snapshots. Color code: Mo: purple, S: yellow, H: white, O: red.

Initially, water molecules from the bulk adsorbed onto Mo sites without dissociation (till ~0.235 ps). Shortly thereafter (at ~0.397 ps), a nearby sulfur atom extracted a proton, leading to water dissociation into OH^- and H^+. The proton migrated to the sulfur atom, forming an S-H bond, while the OH^- bound to Mo. Subsequent snapshots (~0.453-0.456 ps) showed further O-H bond cleavage and S-H formation, resulting in the functionalization of two Mo and two S atoms. At 0.759 ps, another water molecule donated a proton to the surrounding water, generating H_3O^+ and leaving behind a Mo-OH group. Simultaneously, an adjacent water molecule bound to a Mo atom underwent double deprotonation, with one proton binding to a nearby sulfur atom to form S-H, while the other transferred to bulk water and produced a second H_3O^+. Over 28 ps, these processes continued, resulting in the hydrogenation of sulfur sites, Mo functionalization with three oxygen atoms and two OH groups, and non-dissociative adsorption of two water molecules within the hexagonal nanopore.

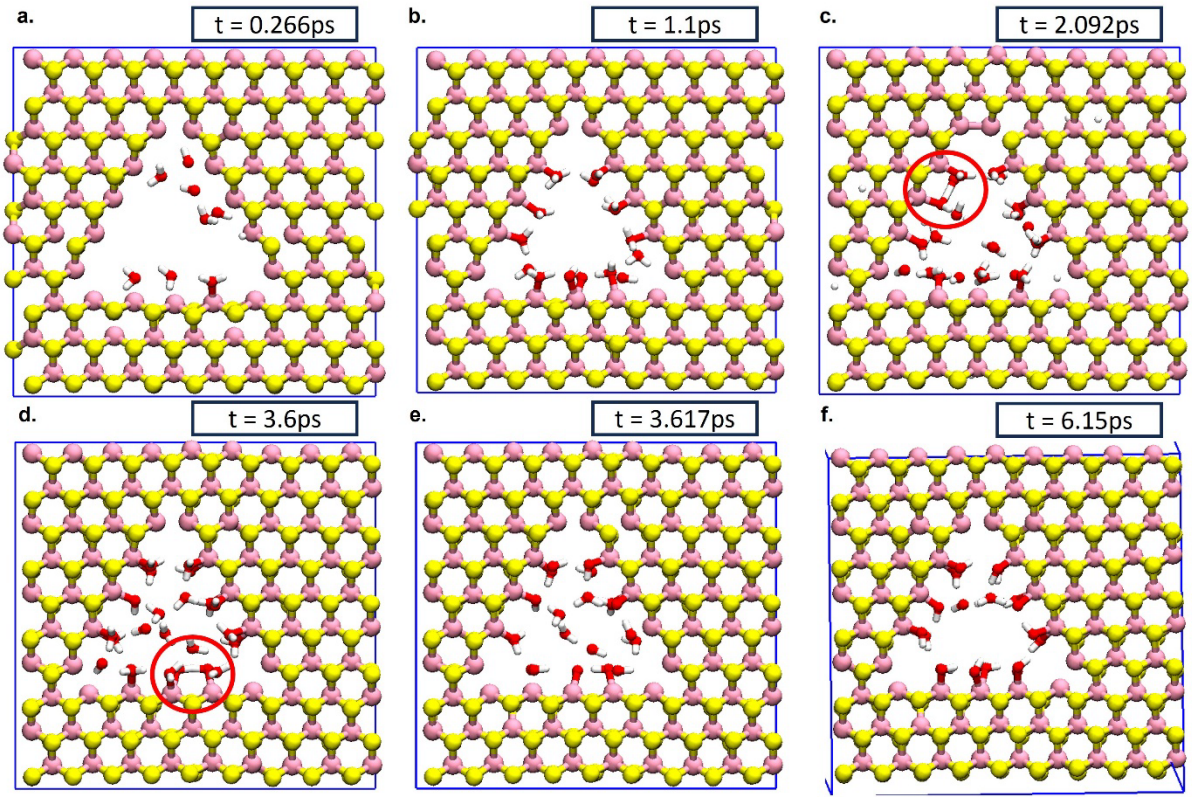

Figure S12. Spin-polarized AIMD simulation snapshots of functionalization of a triangular pore configuration, where only Mo atoms are exposed to the water medium. The simulation time corresponding to each snapshot is indicated in the top right corner. We only show Mo, S, O, and H atoms within 14 Å < z < 18.5 Å to highlight the edge functional groups, with the 2D MoS_2 membrane located in the region 14.6 Å < z < 17.6 Å. Important transitions are marked with red circles in the respective snapshots. Color code: Mo: purple, S: yellow, H: white, O: red.

AIMD simulations of a triangular Mo-terminated pore show that around 0.266 ps, a water molecule from the bulk adsorbs onto a Mo atom without dissociating (Figure S12a). By 1.1 ps, water molecules from the bulk have adsorbed onto all available Mo sites. Subsequently, at approximately 2.092 ps, a nearby water molecule extracts a proton from one of the adsorbed water molecules, initiating its dissociation into H^+ and OH^-. The released proton transfers to the adjacent water molecule, forming H_3O^+, while the remaining OH^- binds to the Mo atom (Figure S12c,d). At 6.15 ps, four Mo atoms are each bonded to OH groups, while two additional water molecules are observed bound to other Mo sites. Overall, this process of proton transfer and bond formation continues over the total 19 ps of AIMD simulation, ultimately resulting in four Mo-OH bonds and the non-dissociative adsorption of two additional water molecules on 5 Mo atoms.

Table S4. Formation energies from DFT to evaluate the stability of the functionalized structures. *X* refers to the nanoporous MoS_2 sheet.

Case	Type	Reaction	Relative formation energy per functionalized atom (eV)
A	Functionalized hexagonal pore	$X + 6H_2O \rightarrow XO_6H_{12}$	-0.762
B	Functionalized Mo-terminated triangular pore	$X + 12H_2O \rightarrow X(OH)_{12} + 12(H^+ + e^-)$	-1.843

The DFT reference energies for water (H_2O) and hydrogen (H_2) were determined by modelling a single molecule in an oversized vacuum box, thereby minimizing spurious interactions and yielding accurate isolated-molecule energies. As per the computational hydrogen electrode approach, the energy of the proton-electron couple is considered to be half that of molecular hydrogen.[15] Note that all DFT calculations described above were performed using the cp2k package.

S6. Potential energy surface fitting for various functionalizations in 2D MoS_2.

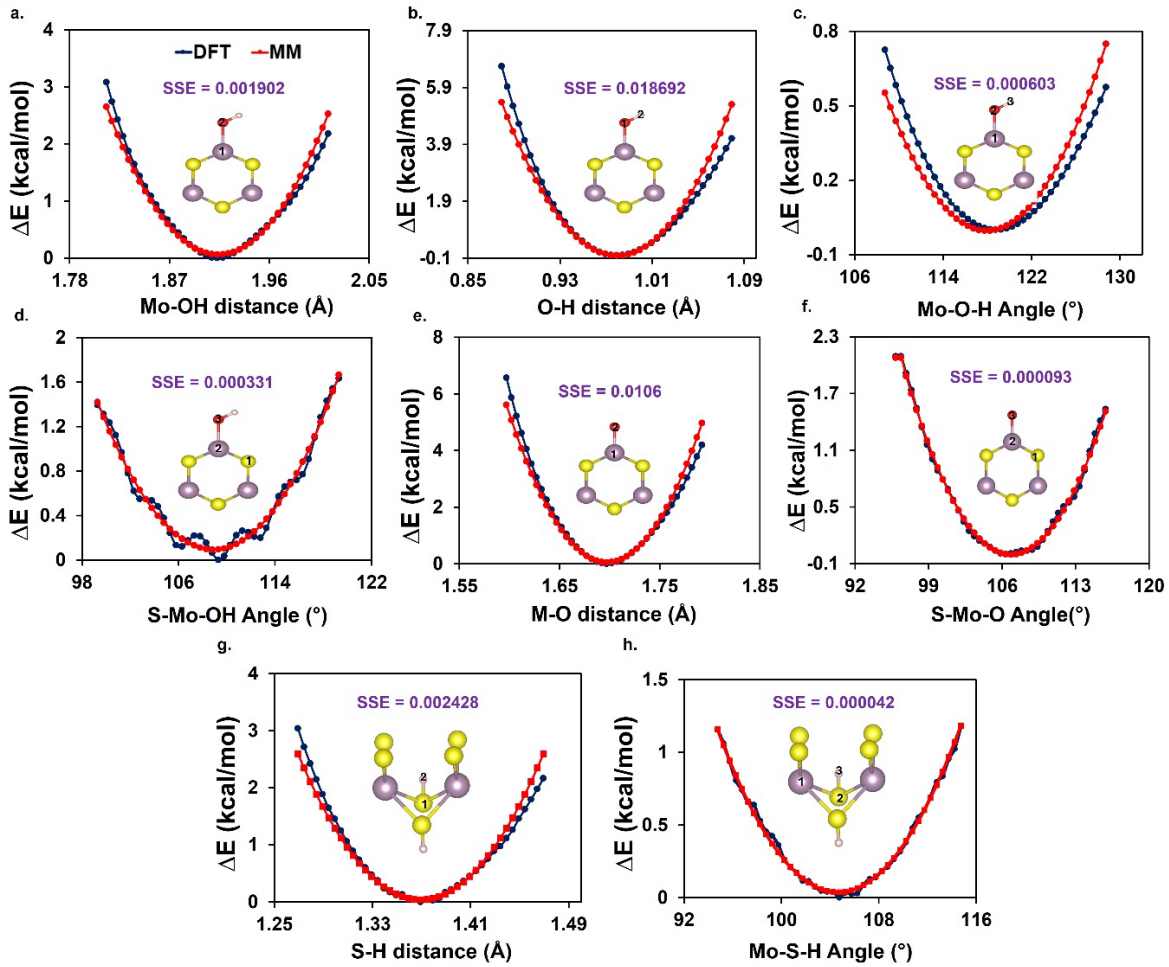

Figure S13. Quality of fitting for the bonded force-field parameters in functionalized MoS_2. Potential energy comparison plots for (a) Mo-O bond in Mo-OH, (b) O-H bond, (c) Mo-O-H angle in Mo-OH, (d) S-Mo-O angle in Mo-OH, (e) Mo-O bond in Mo-O, (f) S-Mo-O angle in Mo-O, (g) S-H bond and (h) Mo-S-H angle. We used a step size of 0.005 Å with 20 steps in either direction for the bonds and a step size of 0.5º with 20 steps in either direction for the angles. The blue data points are from DFT calculations, and the red data points represent the fitted values obtained from GULP based on molecular mechanics calculations (MM). The sum of squared errors (SSE), along with the selected atom sequences for bond and angle variations across different fitting cases, are provided alongside the corresponding fitted plots.

S7. Effect of applied pressure on MD simulation results through MoS_2 nanopores

Table S5. Water permeance and salt rejection performance with an MoS_2 pore.

Functionalized hexagonal pore	**25 MPa**	**50 MPa**
Water permeance (L cm^{-2} MPa^{-1} day^{-1})	44.2 ± 3.7	46.1 ± 2.2
Salt rejection (%)	98.2 ± 0.7	97.7 ± 0.9
Functionalized Mo triangular pore	**25 MPa**	**50 MPa**
Water permeance (L cm^{-2} MPa^{-1} day^{-1})	22.7 ± 2.3	25.3 ± 1.1
Salt rejection (%)	94.9 ± 1.3	94.4 ± 0.7
S-terminated triangular pore	**25 MPa**	**50 MPa**
Water permeance (L cm^{-2} MPa^{-1} day^{-1})	44.0 ± 6.0	43.4 ± 3.3
Salt rejection (%)	99.2 ± 0.6	99.2 ± 0.5

S8. Statistical evaluation of water permeance and salt rejection differences using the Welch t-test, with Holm-Bonferroni correction applied for multiple comparisons

Welch two-sample t-tests[16] were applied to account for unequal variances and sample sizes. First, we computed the t-statistic as follows:

$$t = \frac{\overline{x_1} - \overline{x_2}}{\sqrt{\frac{s_1^2}{n_1} + \frac{s_2^2}{n_2}}}$$

where $\bar{x}_i$, s_i, and n_i denote the sample mean, standard deviation, and sample size of group i, respectively. Next, the degrees of freedom were determined using the Welch-Satterthwaite[17,18] equation as:

$$\nu = \frac{\left(\frac{s_1^2}{n_1} + \frac{s_2^2}{n_2}\right)^2}{\frac{\left(\frac{s_1^2}{n_1}\right)^2}{n_1 - 1} + \frac{\left(\frac{s_2^2}{n_2}\right)^2}{n_2 - 1}}$$

The two-sided p-value was then obtained from the student t distribution[16] as:

$$p = 2[1-F_t\ (|t|; \nu)]$$

where $F_t(\cdot; \nu)$ is the cumulative distribution function of the t-distribution with ν degrees of freedom. An equivalent form is given as:

$$p = 2\,P(T \geq |t|), \qquad T \sim t(\nu)$$

Because multiple pairwise comparisons were performed, p-values were adjusted using the Holm-Bonferroni method. Both raw and corrected p-values are reported. The Holm-Bonferroni-corrected[19] p-value for the i-th hypothesis is calculated as $p_{\text{Holm},i} = \max_{1 \leq j \leq i} [(m - j + 1)\, p_{(j)}]$, where m is the total number of hypotheses tested (total pairwise comparisons), $p_{(j)}$is the j-th smallest raw p-value among all m tests, i is the rank of the hypothesis being considered in the ordered list of p-values. Note that m = 10 in the present study.

Table S6. Pairwise statistical comparison of water permeance among functionalized and unfunctionalized hexagonal and triangular nanopores in MoS_2.

Rank	Pore type 1	Pore type 2	Raw p value	Corrected p (p_{Holm})	Significant after correction
1	Functionalized triangular Mo pore	Unfunctionalized triangular Mo pore	0.00000032	0.00000320	YES
2	Functionalized hexagonal pore	Functionalized triangular Mo pore	0.00000166	0.00001494	YES
3	Unfunctionalized triangular Mo pore	Unfunctionalized triangular S pore	0.00000328	0.00002624	YES
4	Functionalized hexagonal pore	Unfunctionalized triangular Mo pore	0.000009	0.00006300	YES
5	Functionalized triangular Mo pore	Unfunctionalized hexagonal pore	0.0000168	0.00010080	YES
6	Functionalized triangular Mo pore	Unfunctionalized triangular S pore	0.000224	0.00112000	YES
7	Unfunctionalized hexagonal pore	Unfunctionalized triangular Mo pore	0.00052	0.00208000	YES

8	Unfunctionalized hexagonal pore	Unfunctionalized triangular S pore	0.020242	0.06072609	NO
9	Functionalized hexagonal pore	Unfunctionalized hexagonal pore	0.0382	0.07630846	NO
10	Functionalized hexagonal pore	Unfunctionalized triangular S pore	0.506	0.50666529	NO

Table S7. Pairwise statistical comparison of salt rejection among functionalized and unfunctionalized hexagonal and triangular nanopores in MoS_2.

Rank	Pore type 1	Pore type 2	Raw p value	Corrected p (p_{Holm})	Significant after correction
1	Functionalized triangular Mo pore	Unfunctionalized triangular S pore	0.0001543	0.001543	YES
2	Unfunctionalized triangular Mo pore	Unfunctionalized triangular S pore	0.001407	0.0126	YES
3	Unfunctionalized hexagonal pore	Unfunctionalized triangular S pore	0.0079	0.0634	NO
4	Functionalized hexagonal pore	Functionalized triangular Mo pore	0.0163	0.1141	NO
5	Functionalized hexagonal pore	Unfunctionalized triangular Mo pore	0.0251	0.151	NO
6	Functionalized triangular Mo pore	Unfunctionalized hexagonal pore	0.15378	0.7689	NO
7	Unfunctionalized hexagonal pore	Unfunctionalized triangular Mo pore	0.1647	0.6591	NO
8	Functionalized hexagonal pore	Unfunctionalized triangular S pore	0.21167	0.635	NO
9	Functionalized hexagonal pore	Unfunctionalized hexagonal pore	0.2266	0.4532	NO
10	Functionalized triangular Mo pore	Unfunctionalized triangular Mo pore	0.7997	0.7997	NO

S9. Force field robustness under diverse environmental conditions

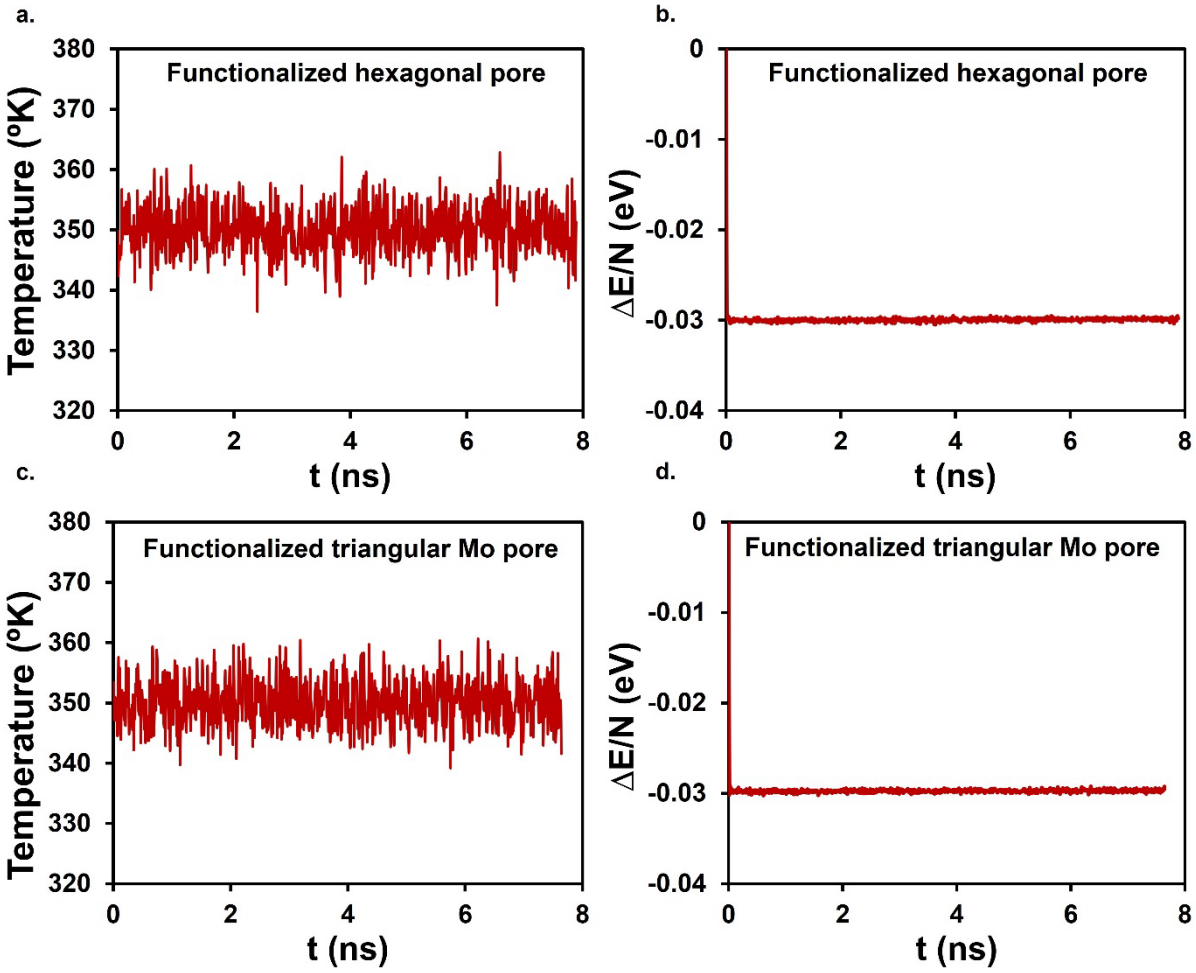

Figure S15. MD simulation results at elevated temperature. (a,c) The temperature fluctuations over the simulation time for the functionalized hexagonal and triangular Mo pores, respectively. (b,d) Total relative energy in eV, normalized by the number of atoms in the system, as a function of simulation time.

References

(1) Goedecker, S.; Teter, M.; Hutter, J. Separable Dual-Space Gaussian Pseudopotentials. *Phys. Rev. B* **1996**, *54* (3), 1703–1710.

(2) Perdew, J. P.; Burke, K.; Ernzerhof, M. Generalized Gradient Approximation Made Simple. *Phys. Rev. Lett.* **1996**, *77* (18), 3865–3867.

(3) Schonfeld, B. B.; Huang, J. J.; Moss, S. C. Anisotropic Mean-Square Displacements (MSD) in Single-Crystals of 2H-MoS_2 And 3R-MoS_2. *Acta Crystallogr.* **1983**, *39*, 404–407.

(4) Lauritsen, J. V.; Kibsgaard, J.; Helveg, S.; Topsøe, H.; Clausen, B. S.; Lægsgaard, E.; Besenbacher, F. Size-Dependent Structure of MoS_2 Nanocrystals. *Nat. Nanotechnol.* **2007**, *2* (1), 53–58. https://doi.org/10.1038/nnano.2006.171.

(5) Byskov, L. S.; Nørskov, J. K.; Clausen, B. S.; Topsøe, H. Edge Termination of MoS_2 and CoMoS Catalyst Particles. *Catal. Lett.* **2000**, *64*, 95–99.

(6) Blöchl, P. E. Electrostatic Decoupling of Periodic Images of Plane-Wave-Expanded Densities and Derived Atomic Point Charges. *J. Chem. Phys.* **1995**, *103* (17), 7422–7428. https://doi.org/10.1063/1.470314.

(7) Ghorai, S.; Dhondi, P.; Govind Rajan, A. Molecular Dynamics Simulations of Functionalized hBN Nanopores in Water: *Ab Initio* Force Field and Implications for Water Desalination. *J. Chem. Phys.* **2025**, *162* (4), 044705. https://doi.org/10.1063/5.0242541.
(8) Manz, T. A.; Limas, N. G. Introducing DDEC6 Atomic Population Analysis: Part 1. Charge Partitioning Theory and Methodology. *RSC Adv.* **2016**, *6* (53), 47771–47801. https://doi.org/10.1039/c6ra04656h.
(9) Limas, N. G.; Manz, T. A. Introducing DDEC6 Atomic Population Analysis: Part 2. Computed Results for a Wide Range of Periodic and Nonperiodic Materials. *RSC Adv.* **2016**, *6* (51), 45727–45747. https://doi.org/10.1039/c6ra05507a.
(10) Zeron, I. M.; Abascal, J. L. F.; Vega, C. A Force Field of Li^+, Na^+, K^+, Mg^{2+}, Ca^{2+}, Cl^-, and SO_4^{2-} In Aqueous Solution Based on the TIP4P/2005 Water Model and Scaled Charges for the Ions. *J. Chem. Phys.* **2019**, *151* (13), 134504. https://doi.org/10.1063/1.5121392.
(11) Cheng, A.; Steele, W. A. Computer Simulation of Ammonia on Graphite. I. Low Temperature Structure of Monolayer and Bilayer Films. *J. Chem. Phys.* **1990**, *92* (6), 3858–3866. https://doi.org/10.1063/1.458562.
(12) Sresht, V.; Rajan, A. G.; Bordes, E.; Strano, M. S.; Pádua, A. A. H.; Blankschtein, D. Quantitative Modeling of MoS_2 –Solvent Interfaces: Predicting Contact Angles and Exfoliation Performance Using Molecular Dynamics. *J. Phys. Chem. C* **2017**, *121* (16), 9022–9031. https://doi.org/10.1021/acs.jpcc.7b00484.
(13) Abascal, J. L. F.; Vega, C. A General Purpose Model for the Condensed Phases of Water: TIP4P/2005. *J. Chem. Phys.* **2005**, *123* (23), 234505. https://doi.org/10.1063/1.2121687.
(14) Ghuman, K. K.; Yadav, S.; Singh, C. V. Adsorption and Dissociation of H_2 O on Monolayered MoS_2 Edges: Energetics and Mechanism from *Ab Initio* Simulations. *J. Phys. Chem. C* **2015**, *119* (12), 6518–6529. https://doi.org/10.1021/jp510899m.
(15) Nørskov, J. K.; Rossmeisl, J.; Logadottir, A.; Lindqvist, L.; Kitchin, J. R.; Bligaard, T.; Jónsson, H. Origin of the Overpotential for Oxygen Reduction at a Fuel-Cell Cathode. *J. Phys. Chem. B* **2004**, *108* (46), 17886–17892. https://doi.org/10.1021/jp047349j.
(16) Welch, B. L. THE GENERALIZATION OF 'STUDENT'S' PROBLEM WHEN SEVERAL DIFFERENT POPULATION VARLANCES ARE INVOLVED. *Biometrika* **1947**, *34* (1–2), 28–35. https://doi.org/10.1093/biomet/34.1-2.28.
(17) Satterthwaite, F. E. An Approximate Distribution of Estimates of Variance Components. *Biom. Bull.* **1946**, *2* (6), 110. https://doi.org/10.2307/3002019.
(18) Ruxton, G. D. The Unequal Variance T-Test Is an Underused Alternative to Student's t-Test and the Mann–Whitney U Test. *Behav. Ecol.* **2006**, *17* (4), 688–690. https://doi.org/10.1093/beheco/ark016.
(19) Holm, S. A Simple Sequentially Rejective Multiple Test Procedure. *Scand. J. Stat.* **1979**, *6*, 65–70. https://doi.org/10.2307/4615733.